Optical Engineering

SPIEDigitalLibrary.org/oe

Study of a constructed function for approximating mode field in photonic crystal fibers

Lu Zhang
Zhiyong Wu
Shijie Gao
Ming Cui

Study of a constructed function for approximating mode field in photonic crystal fibers

Lu Zhang
Changchun Institute of Optics, Fine Mechanics and Physics
Chinese Academy of Sciences
Changchun 130033, China
and
Graduate University of the Chinese Academy of Sciences
Beijing 100049, China
E-mail: LZhangpai@gmail.com

Zhiyong Wu
Shijie Gao
Changchun Institute of Optics, Fine Mechanics and Physics
Chinese Academy of Sciences
Changchun 130033, China

Ming Cui
Changchun Institute of Optics, Fine Mechanics and Physics
Chinese Academy of Sciences
Changchun 130033, China
and
Graduate University of the Chinese Academy of Sciences
Beijing 100049, China

Abstract. A function is constructed to approximate the fundamental mode field precisely in photonic crystal fibers (PCFs) using least square error criteria. Through the unconstrained nonlinear programming method, the optimum parameters of the constructed function are derived, and the optimum constructed function is found. For photonic crystal fibers, using such an optimum constructed function, small errors are brought out when approximating their fundamental mode fields regardless of d/Λ values. Furthermore, the constructed function is not only suitable for index-guiding PCFs, but also for bandgap PCFs with hollow core to some extent. Based on this constructed function, an analytic expression for the far field of the approximated fundamental mode field is deduced. Numerical results demonstrate that the analytic expression brings out small errors compared with the actual far field. [DOI: 10.1117/1.OE.51.6.065003]

Subject terms: photonic crystal fibers; fundamental mode filed; approximation; constructed function; far field.

Paper 111583 received Dec. 15, 2011; revised manuscript received Apr. 13, 2012; accepted for publication Apr. 27, 2012; published online Jun. 5, 2012.

1 Introduction

Photonic crystal fibers (PCFs) have a silica core in their center and air holes in their cladding. Light in such PCFs is guided by total internal reflection caused by the effective index difference between the core and the cladding, so the light can be trapped in the core.[1] Because the effective refractive index of the cladding is affected by the holes diameter d and the hole-to-hole spacing Λ, the characters of such PCFs can be varied by changing d and Λ.[2,3] For example, the fundamental mode field distribution is varied by changing d and Λ.

For standard step-index fibers (SIFs) and PCFs, the analytic expression of the fundamental mode field is important in estimating the splice loss, free space to fiber coupling efficiency, and reflection.[4] The mode field of SIFs can be approximated by a Gaussian function precisely. Based on such an analytic expression, the free space to fiber coupling efficiency has been studied extensively.[5–11] Recently, PCFs have been widely used in stellar interferometers. But due to the difficulty in obtaining the analytic expression of PCF's fundamental mode field, the numerical method had been utilized to study the free space to PCF coupling efficiency.[12–15] Using the Gaussian function merely to approximate the PCF's fundamental mode field may not always be valid.[16–18] Furthermore, Hirooka et al. have reported that approximating the fundamental mode fields of PCFs with small d/Λ values by Gaussian function brought out large errors.[4] Therefore, they proposed that the Gaussian function be replaced by hyperbolic-secant (Sech) function for PCFs with small d/Λ values, but for PCFs with large d/Λ values, the Gaussian function should still be used. An analytical model for the mode of index-guided microstructure fibers was previously proposed by Sharma and Chauhan.[19] A variational method was utilized to obtain the parameters of the analytical model. Furthermore, the propagation constant was also obtained, thus, the modal effective index and the dispersion parameters were calculated to verify the validity of the analytical model. The variational approach was also utilized by Ghosh et al. to determine the modal effective indices and dispersion of microstructure fibers.[20] A simple Gaussian function and modified Bessel function were considered for the core and cladding, respectively.

To obtain a precise analytic expression of the fundamental mode field of PCF regardless of d/Λ value, this paper proposes a constructed function that, no matter what the value of d/Λ, generates little error when approximating the fundamental mode field of PCF. Furthermore, this constructed function is not only suitable for the index-guiding PCFs, but also for bandgap PCFs with hollow core to some extent. In addition, because of the circular symmetry of the constructed function, an analytical expression for the far field of the approximated fundamental mode field is easily obtained.

0091-3286/2012/$25.00 © 2012 SPIE

2 Characters of the Fundamental Mode Fields in PCFs

The finite difference time domain (FDTD) method[21] is utilized to calculate the mode field of the HE_{11} mode of PCF. For different d/Λ values, the mode fields are shown in Fig. 1. The parameters used in the computation are wavelength $\lambda = 1.55$ μm, hole-to-hole spacing $\Lambda = 2.3$ μm, hole diameter $d = 0.46$ μm [Fig. 1(a)], 0.69 μm [Fig. 1(b)], 0.92 μm [Fig. 1(c)], 1.15 μm [Fig. 1(d)], 1.38 μm [Fig. 1(e)], 1.61 μm [Fig. 1(f)].

From Fig. 1(a), 1(b), and 1(c), it is seen that for small d/Λ values the mode fields distribute widely, and much of the field energy distributes around the air-holes. Hence, the mode fields have many dips. Figure 1(d), 1(e), and 1(f) shows that for large d/Λ values most of the mode field energy is trapped in the core, and the mode fields have few dips. In short, the distribution of the mode fields with small d/Λ values is apparently different from that of mode fields with large d/Λ values. To approximate the mode field better, the above characters should be considered necessarily.

3 Theoretical Basis

In our pervious paper,[22] we defined the magnitude response of one stage Butterworth filter as

$$|H(j\omega)| = \frac{1}{1+\gamma(\omega/\omega_c)^2}, \tag{1}$$

where ω_c was the cutoff frequency of the ideal Gaussian filter and γ was an adjustable coefficient. According to Wells,[23] an ideal Gaussian filter can be approximated by cascading uniform filters. Consequently, in our previous paper,[22] we proposed to approximate the Gauss filter by cascading the Butterworth filters in Eq. (1). Thus, the relationship between the Gauss filter and the Butterworth filter can be given by Ref. 22

$$|G(j\omega)| = \exp(-a^2\omega^2) = \lim_{M\to\infty}\left[\frac{1}{1+\gamma(\omega/\omega_c)^2}\right]^M, \tag{2}$$

where M is the stage number of cascading Butterworth filters, and M is a positive integer.

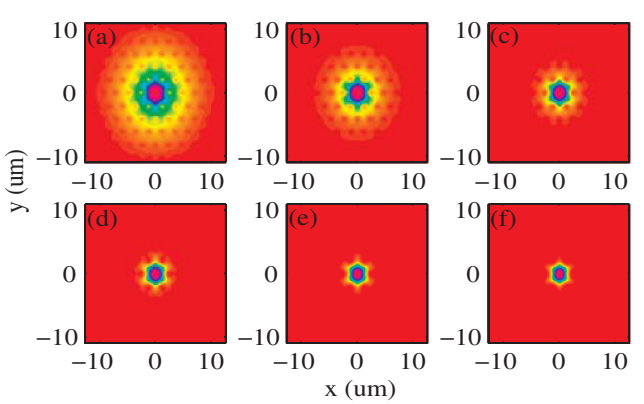

Fig. 1 Field distribution of the fundamental mode field of PCF with (a) $d=0.46\mu$m($d/\Lambda=0.2$), (b) 0.69μm($d/\Lambda=0.3$) (c) 0.92μm ($d/\Lambda=0.4$) (d) 1.15 μm($d/\Lambda=0.5$) (e) 1.38 μm($d/\Lambda=0.6$) (f) 1.61 μm($d/\Lambda=0.7$).

For the two dimensional Gauss function, Eq. (2) can be written as

$$g(x,y) = \exp\left(-\frac{x^2+y^2}{\omega^2}\right) = \lim_{M\to\infty}\left[\frac{1}{1+\xi\cdot(x^2+y^2)}\right]^M, \tag{3}$$

where M is relaxed to $M \in \mathbb{R}^+$, and $\mathbb{R}^+$ means positive real number. According to Eq. (3), the function $f(x,y) = [1+\xi\cdot(x^2+y^2)]^{-M}$ can be utilized to approximate the two dimensional Gauss function. Adjusting the parameters ξ and M, the error between the Gauss function and $f(x,y)$ varies and the shape of $f(x,y)$ can be changed. Despite of the complicated fundamental mode field profile of PCFs with different structures, the function $f(x,y)$ with adjusting parameters ξ and M can be utilized to approximate the fundamental mode fields of the PCFs.

4 Constructing an Approximation Function

Based on the above theoretical basis, a function is constructed in the form of

$$f(x,y) = \left[\frac{1}{1+\xi(x^2+y^2)}\right]^M, \tag{4}$$

where ξ, $M \in \mathbb{R}^n$ and $\xi \in (0,+\infty)$, $M \in (0,+\infty)$. In the intervals of $\xi \in (0,+\infty)$ and $M \in (0,+\infty)$, $f(x,y)$ possesses continuous first and second partial derivatives with respect to ξ and M.

The actual mode field of PCF is assumed to be $\phi(x,y)$. The least square error between $f(x,y)$ and $\phi(x,y)$ can be defined as

$$\begin{aligned} I(\xi,M) &= \int_{-\infty}^{+\infty}\int_{-\infty}^{+\infty}[\phi(x,y)-f(x,y)]^2\mathrm{d}x\mathrm{d}y \\ &= \int_{-\infty}^{+\infty}\int_{-\infty}^{+\infty}\{\phi(x,y)-[1+\xi(x^2+y^2)]^{-M}\}^2\mathrm{d}x\mathrm{d}y. \end{aligned} \tag{5}$$

Because $f(x,y)$ possesses continuous first and second partial derivatives with respect to ξ and M in the intervals of $\xi \in (0,+\infty)$ and $M \in (0,+\infty)$, hence, $I(\xi,M)$ also possesses continuous first and second partial derivatives with respect to ξ and M in the same intervals. The key to construct $f(x,y)$ is to derive ξ_{opt} and M_{opt}, which minimize $I(\xi,M)$. Then, the optimum approximation function $f_{\mathrm{opt}}(x,y)$ can be obtained.

In the intervals of $\xi \in (0,+\infty)$ and $M \in (0,+\infty)$, deriving ξ_{opt} and M_{opt} which minimize $I(\xi,M)$ can be considered as constrained nonlinear programming, which can be represented in the form

$$\min I(\xi,M) \quad s.t.\xi > 0 \quad M > 0, \tag{6}$$

where $I(\xi,M)$ is objective function, $\xi > 0$ and $M > 0$ are constraints, $s.t.$ means "subject to." To resolve Eq. (6), let us define a new objective function by combining all the constraints as the Lagrangian function,[24] then the Lagrangian function is

$$L(\xi,M,\mu_1,\mu_2) = I(\xi,M) + \mu_1\cdot(-\xi) + \mu_2\cdot(-M), \tag{7}$$

where ξ, M, μ_1, and μ_2 are decision variables. According to the first-order Kuhn-Tucker necessary condition,[24] at the local optimum solutions, there is

$$\nabla L(\xi_{\text{opt}}, M_{\text{opt}}, \mu_1^*, \mu_2^*) = \nabla I(\xi_{\text{opt}}, M_{\text{opt}}) + \mu_1^* \times \nabla(-\xi) + \mu_2^* \times \nabla(-M) = 0, \tag{8}$$

with μ_1^*, $\mu_2^* \geq 0$ and ∇ refers to gradient operator. After executing Eq. (8), the necessary condition becomes

$$\begin{cases} \frac{\partial L}{\partial \xi} = \left.\frac{\partial I(\xi,M)}{\partial \xi}\right|_{(\xi_{\text{opt}}, M_{\text{opt}})} - \mu_1^* = 0 \\ \frac{\partial L}{\partial M} = \left.\frac{\partial I(\xi,M)}{\partial M}\right|_{(\xi_{\text{opt}}, M_{\text{opt}})} - \mu_2^* = 0 \end{cases}. \tag{9}$$

It has been verified that the intervals of optimum solutions satisfying Eq. (9) are $\xi_{\text{opt}} > 0$ and $M_{\text{opt}} > 1/2$ (see Appendix A). As a result, the form of the constrained nonlinear programming is rewritten as

$$\min\ I(\xi, M) \quad s.t. \xi > 0 \quad M > 1/2. \tag{10}$$

To resolve such constrained nonlinear programming in Eq. (10), penalty methods or feasible direction methods[25] can be used. But Eq. (10) can also be treated as unconstrained nonlinear programming. The verifications are given successively.

It is assumed that the intervals of ξ and M in $f(x, y)$ are ξ, $M \in \mathbb{R}^n$. Therefore, deriving $(\xi_{\text{opt}}, M_{\text{opt}})$ which minimizing $I(\xi, M)$ can be represented as unconstrained nonlinear programming in the form of

$$\min\ I(\xi, M) \quad s.t. \xi \in \mathbb{R}^n \quad M \in \mathbb{R}^n. \tag{11}$$

We assume that $I(\xi, M)$ possesses continuous first and second partial derivatives with respect to ξ_{opt} and M_{opt}. According to the first-order necessary condition of unconstrained nonlinear programming,[24] at local optimum solutions $(\xi_{\text{opt}}, M_{\text{opt}})$, $\nabla I(\xi_{\text{opt}}, M_{\text{opt}}) = 0$ must be satisfied, namely

$$\begin{cases} \left.\frac{\partial I(\xi,M)}{\partial \xi}\right|_{(\xi_{\text{opt}}, M_{\text{opt}})} = 0 \\ \left.\frac{\partial I(\xi,M)}{\partial M}\right|_{(\xi_{\text{opt}}, M_{\text{opt}})} = 0 \end{cases}. \tag{12}$$

It has been verified that the intervals of optimum solutions satisfying Eq. (12) are also $\xi_{\text{opt}} > 0$ and $M_{\text{opt}} > 1/2$ (see Appendix B). Consequently, all the optimum solutions minimizing $I(\xi, M)$ lie in the intervals $\xi \in (0, +\infty)$ and $M \in (1/2, +\infty)$. So treating Eq. (10) as unconstrained nonlinear programming cannot miss the optimum solutions. To simplify the solving process, we treat Eq. (10) as unconstrained nonlinear programming.

For the unconstrained nonlinear programming above, the second-order sufficiency conditions[24]

$$\begin{cases} J = \nabla I(\xi_{\text{opt}}, M_{\text{opt}}) = 0 \\ H = \nabla^2 I(\xi_{\text{opt}}, M_{\text{opt}}), H \text{ is positive definite} \end{cases} \tag{13}$$

must be satisfied. In Eq. (13), J is Jacobian vector and H is Hessian matrix. After solving Eq. (13), strong local optimum solutions $(\xi_{\text{opt}}, M_{\text{opt}})$ can be obtained. But solving the above sufficiency conditions has to use special numerical algorithm. In this paper, we use the Davidon-Fletcher-Powell method.[25] Then, a group of strong local optimum solutions satisfying Eq. (13) for PCFs with different d/Λ values are obtained in Table 1. Table 1 also shows the least square errors between the actual mode fields and the approximated mode fields by the optimum constructed function. Seen from Table 1, all the optimum solutions lie in $\xi \in (0, +\infty)$ and $M \in (1/2, +\infty)$. Thus, the optimum constructed functions are obtained for PCFs with different d/Λ values using these optimum parameters.

5 Numerical Results of the Constructed Function

5.1 *Results of the Total Internal Reflection PCFs with Circular Air Holes*

For comparison, the Gaussian (Gauss) function,[4] hyperbolic-secant (Sech) function[4] and the constructed function proposed here are utilized to approximate the fundamental mode fields of PCFs, which have different d/Λ values. The least square errors arisen from Gauss, Sech, and constructed function, respectively are tabulated in Table 2.

By interpolating the data points in Table 2, the curves of least square errors are obtained and plotted in Fig. 2.

Both Table 2 and Fig. 2 indicate that the constructed function causes smaller errors compared with Gauss and Sech function when the mode fields of PCFs with small d/Λ values are approximated. For PCFs with large d/Λ values, the errors caused by the constructed function and Gaussian function are very close and small; they are both smaller than the errors caused by Sech function. The constructed function can be observed to approximate PCFs better because it not only brings out small errors, but also just uses one function to approximate the mode fields of PCFs regardless of d/Λ values.

For further comparison, the profiles of the mode fields of PCFs with $d/\Lambda = 0.2$ and $d/\Lambda = 0.6$ are approximated by using the Gaussian function, Sech function, and constructed function, respectively. Figure 3 shows $d/\Lambda = 0.2$ and Fig. 4 shows $d/\Lambda = 0.6$. In both Figs. 3 and 4, the x axis is the

Table 1 Optimum parameters and the approximation errors using optimum constructed function.

d/Λ	ξ	M	Least square error
0.2	0.1729	1.1575	0.3432
0.3	0.1983	1.6927	0.1631
0.4	0.1030	4.0095	0.1048
0.5	0.0068	70	0.0534
0.6	0.0122	46	0.0397
0.7	0.0075	90	0.0281
0.8	0.0103	78	0.0217

Table 2 Approximation errors caused by the Gauss, Sech, and constructed function, respectively.

d/Λ	Gauss	Sech	Constructed function
0.2	1.8424	0.9070	0.3432
0.3	0.4813	0.2567	0.1631
0.4	0.1290	0.1337	0.1048
0.5	0.0528	0.1214	0.0534
0.6	0.0377	0.1146	0.0397
0.7	0.0270	0.0996	0.0281
0.8	0.0205	0.0846	0.0217

location along radial direction of the PCF, the y axis of (a) is the linear amplitude. The y axis of (b) is the log amplitude and (c) shows the approximation errors at different locations. The legend of "Actual" means the fundamental mode field profile obtained using FDTD method.

Seen in Fig. 3(a) and 3(b), much of the mode field energy distributes in the interval of -5 to 5 μm. Figure 3(c) shows that the mean approximation errors brought by the constructed function are smaller than that brought by the Gaussian and Sech function in this interval. In the intervals of -10 to 5 μm and 5 to 10 μm, the mean approximation

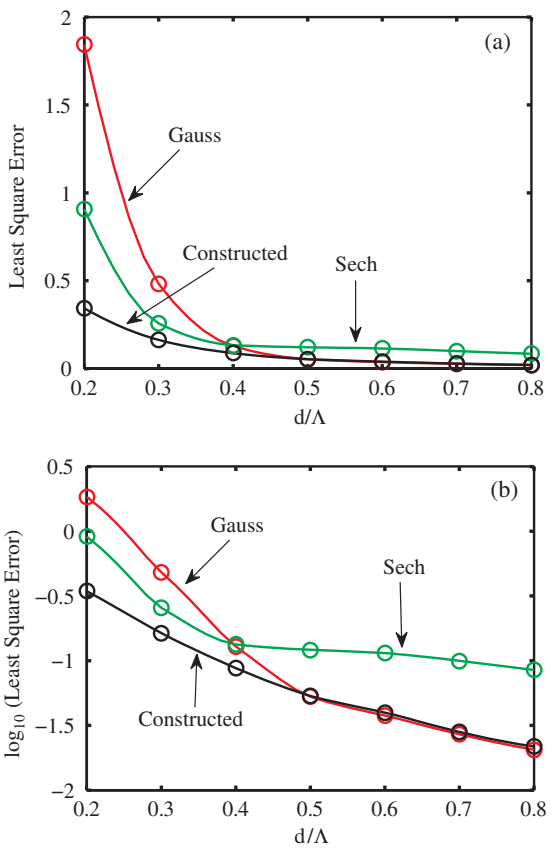

Fig. 2 Least square errors caused by Gauss, Sech, and constructed function. (a) Linear scale, (b) log scale. ($\lambda = 1.55$ μm).

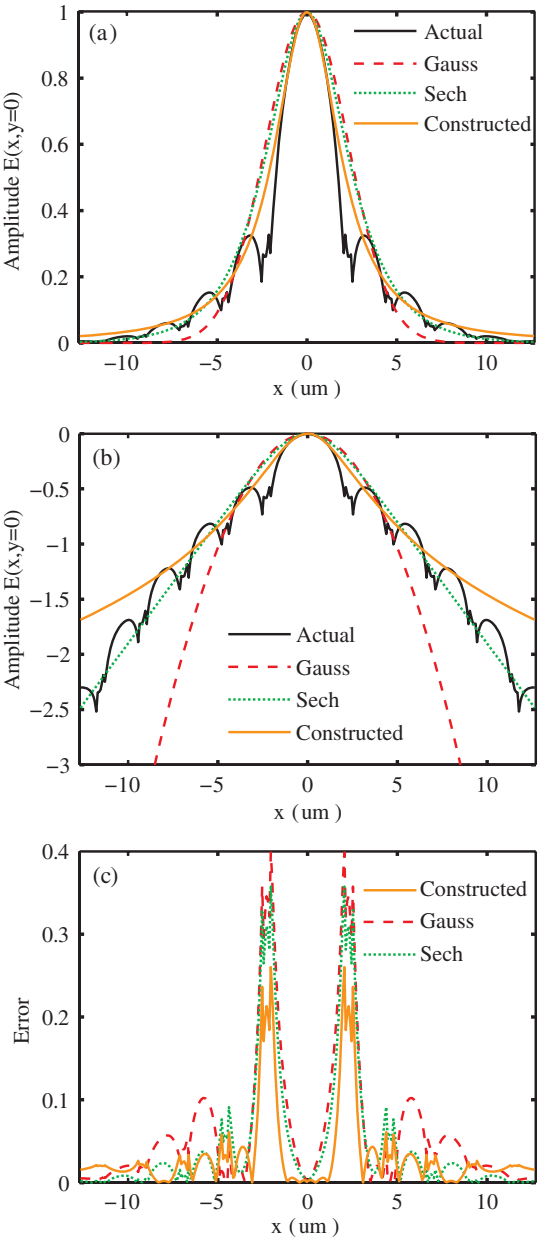

Fig. 3 Comparison of the actual PCF's field profile (black) with Gauss (red), Sech (green), and constructed function (orange) profile for $d/\Lambda = 0.2$. (a) Amplitude with linear scale. (b) Amplitude with log scale. (c) Approximation errors along x axis. The mode field is plotted along x axis.

errors caused by the constructed function are nearly the same as those caused by the Sech function. Additionally, they are both smaller than those caused by Gaussian function. In Fig. 3(c), the integrals of the Gaussian, Sech, and constructed function along x axis are 1.6451, 1.1843, and 0.8425, respectively. So for PCFs with small d/Λ values, the constructed function has the best approximation performance.

In Fig. 4(a) and 4(b), nearly all of the mode field energy distributes in the interval of -5 to 5 μm. Seen from (c), the error curves of the Gaussian function and constructed function nearly overlap in this interval. Hence, their mean approximation errors are nearly equivalent. The errors caused by Sech function are obviously larger than those

caused by Gaussian and constructed function. In Fig. 4(c), the integrals of the Gaussian, Sech, and constructed function along x axis are 0.2221, 0.5112, and 0.2309, respectively. So for PCFs with large d/Λ values, the constructed function and Gaussian function exhibit almost the equivalent approximation performance. Both of their approximation performance is better than that of Sech function.

To emphasize on the utility of our proposed function, the propagation constants are calculated by the proposed function in combination with the variational method in Refs. 19 and 20 firstly. The scalar variational expression for propagation constant β is given[19,20] by

$$\beta^2 = \frac{k_0^2 \int_0^\infty n^2(R)|\psi|^2 R dR - a^{-2} \int_0^\infty |d\psi/dR|^2 R dR}{\int_0^\infty |\psi|^2 R dR}, \quad (14)$$

where ψ is our proposed function here. Then, using β, the modal effective index and dispersion are obtained. The results have been compared with those obtained by a freely available software, CUDOS microstructured optical fibre (MOF) Utilities.[26] The software is based on a multipole method.[27,28] The results are plotted in Fig. 5.

Figure 5(a) and 5(b) shows the comparison of n_{eff} values obtained from the variational method using our proposed function and multipole method for different $f = d/\Lambda$ and Λ, respectively. In fact, it is observed that the results obtained by the proposed function agree well with those obtained using the multipole method.

The dispersion coefficients calculated using the n_{eff} in Fig. 5 are shown in Fig. 6. In Fig. 6(a), these curves show that our proposed function predicts dispersion coefficients reasonably well at lower wavelengths and deviated slightly at longer wavelengths for large f values. The poor confinement of the fundamental mode in the core results in such deviation at longer wavelengths.

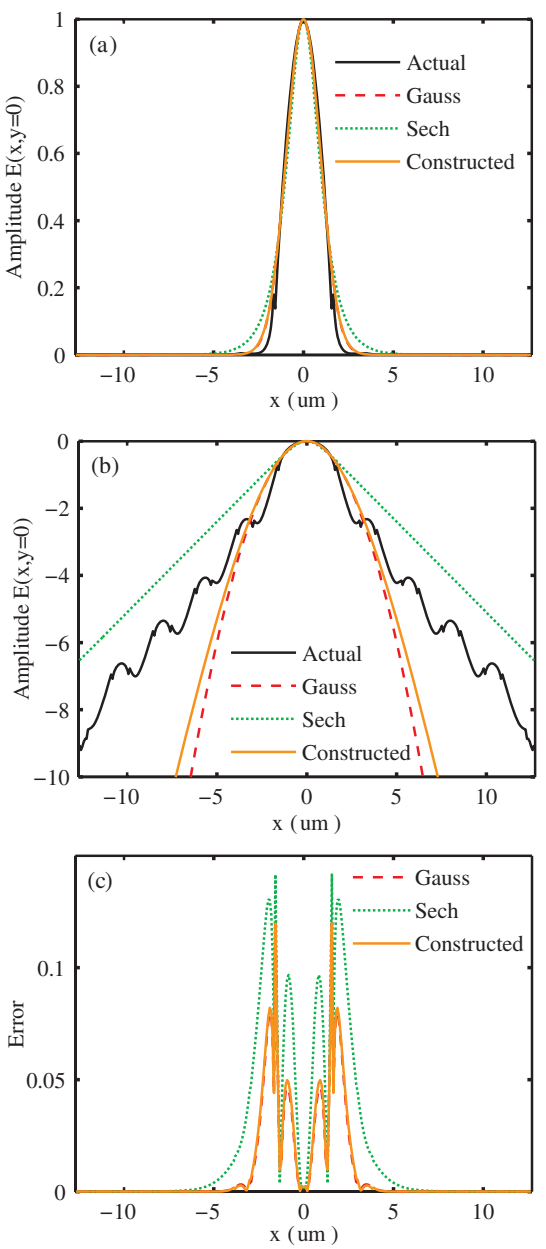

Fig. 4 Comparison of the actual PCF's field profile (black) with Gauss (red), Sech (green), and constructed function (orange) profile for $d/\Lambda = 0.6$. (a) Amplitude with linear scale. (b) Amplitude with log scale. (c) Approximation errors along x axis. The mode field is plotted along x axis.

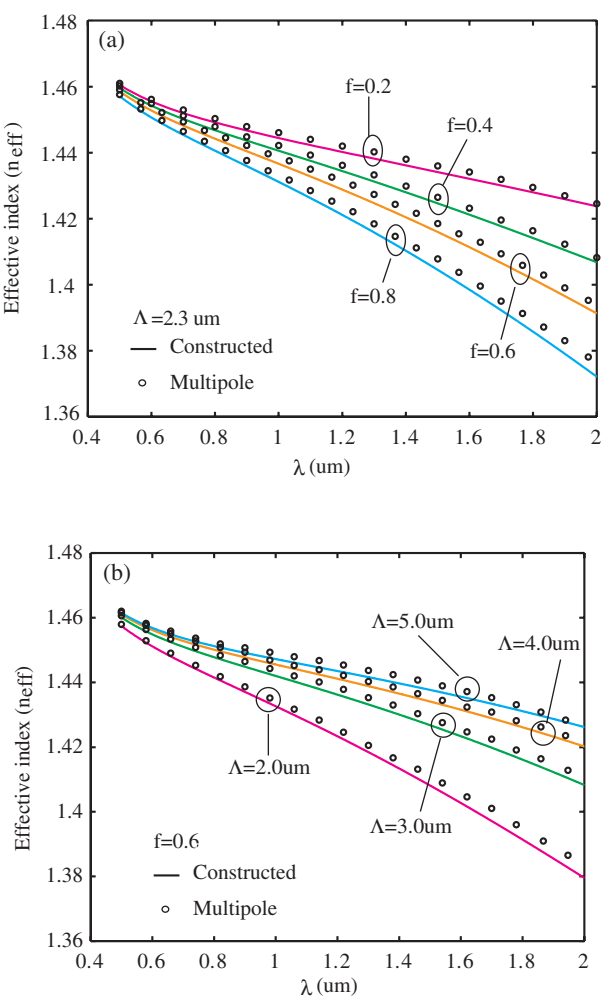

Fig. 5 Plot of n_{eff} with wavelength at (a) constant Λ with varying $f = d/\Lambda$ and (b) constant f with varying Λ for hexagonal lattice microstructured optical fibres (MOFs). The solid lines are obtained by our proposed function in combination with the variational method. The circulars are obtained by the Multipole method in CUDOS MOF Utilities.

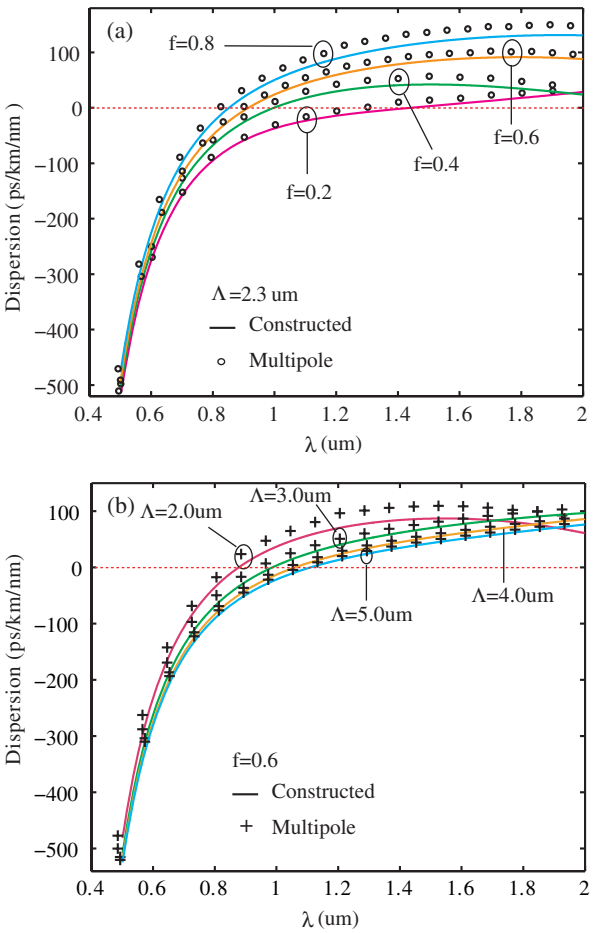

Fig. 6 Dispersion curves obtained by the proposed function in combination with variational method and Multipole method in CUDOS MOF Utilities. (a) constant Λ with varying $f = d/\Lambda$ and (b) constant f with varying Λ for hexagonal lattice MOFs. The solid lines are obtained by our proposed function in combination with the variational method. The circulars and plus signs are obtained by the Multipole method in CUDOS MOF Utilities.

In Fig. 6(b), apart from the curve of $\Lambda = 2.0$ um, other curves obtained from our proposed function and Multipole method match well at $\Lambda = 3.0$ um to $\Lambda = 5.0$ um throughout the entire wavelength span of 0.5 to 2.0 μm. The mismatch for $\Lambda = 2.0$ um at longer wavelengths is also because of the poor confinement of fundamental mode.

5.2 *Results of the Total Internal Reflection PCFs with Elliptical Air Holes*

To further prove the performance of our proposed constructed function, we performed a modal approximation of a three-ring elliptical air hole photonic crystal fiber. The hexagonal PCF considered has three rings of air holes in a triangular lattice arrangement with a pitch $\Lambda = 2.3$ μm. The same configurations of elliptical air holes as in Sharma et al.[29] are used. Hence, three configurations of elliptical air holes are considered, denoted as Configurations I, II, and III. Furthermore, we consider the effect of the rotation of the ellipse axes, so the ellipse axes are rotated by 0 and 90 deg. We use "elliptical 0°" and "elliptical 90°" to represent these two orientations, respectively. These elliptical configurations are shown in Table 3. In Table 3, r_{maj} means the major axis radius of the elliptical hole, r_{min} is

Table 3 Various configurations considered for elliptical air holes.

	Configuration I	Configuration II	Configuration III
Elliptical 0 deg	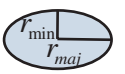		
Elliptical 90 deg			

the minor axis radius. As in Ref. 29, the area of the hole has been preserved, so that $r^2 = r_{maj} \cdot r_{min}$. Accordingly, the elliptical air hole with r_{maj} and r_{min} can be equivalent to the circular air hole with radius r. Thus, $d/\Lambda = 2r/\Lambda$ can be equivalent to the air-filling fraction of the PCF having elliptical holes. Two cases of air-filling fraction are considered here. In the first case, there is $r = 0.345$ μm, namely, $0.345^2 = r_{maj} \cdot r_{min}$, so $d/\Lambda = 0.3$. In the second case, $r = 0.69$ μm, so $d/\Lambda = 0.6$.

For the first case, the fundamental mode fields of PCFs with different elliptical air holes are shown in Fig. 7. Then the Gauss, Sech, and constructed function are utilized to approximate all the fields. The errors for different configurations are tabulated in Table 4. It is observed that the constructed function performs better than the Gauss and Sech function for such $d/\Lambda = 0.3$ case. And it is also seen that the Sech function performs better than the Gauss function here. Consequently, this trend agrees well with that in Table 2 and Fig. 2.

For the second case, the fundamental mode fields and the approximation errors are shown in Fig. 8 and Table 5, respectively. From Table 5, it is observed that for such $d/\Lambda = 0.6$ case the Gauss function has the best performance, the constructed function performs better than the Sech function, and the performance of the constructed function is close to that of the Gauss function. Hence, this trend also matches well with that in Table 2 and Fig. 2.

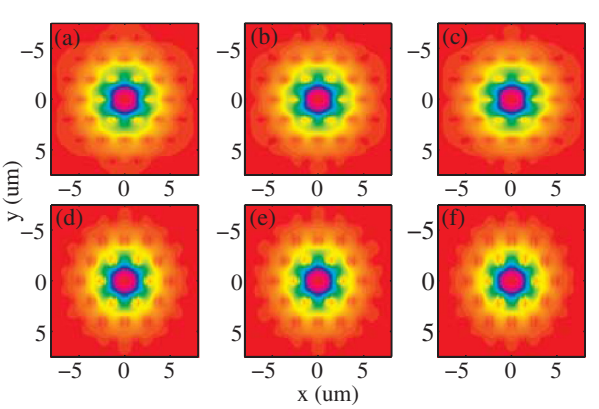

Fig. 7 Fundamental mode fields of PCFs with different elliptical air holes when $r = 0.345$ μm. The orientation of (a)–(c) is 0 deg. The orientation of (d)–(f) is 90 deg. (a) and (d): $r_{maj} = 0.5$ μm, $r_{min} = 0.2361$ μm, (b) and (e): $r_{maj} = 0.45$ μm, $r_{min} = 0.2645$ μm, (c) and (f): $r_{maj} = 0.6$ μm, $r_{min} = 0.19638$ μm.

Table 4 Approximation errors for various configurations and orientations when $r = 0.345\mu$m.

Orientation	Function	Configuration I $r_{maj} = 0.6\ \mu$m, $r_{min} = 0.19638\ \mu$m	Configuration II $r_{maj} = 0.5\ \mu$m, $r_{min} = 0.2361\ \mu$m	Configuration III $r_{maj} = 0.45\ \mu$m, $r_{min} = 0.2645\ \mu$m
0 deg	Gauss	0.6154	0.6631	0.6306
	Sech	0.2827	0.3050	0.2948
	Constructed	0.1607	0.1599	0.1665
90 deg	Gauss	0.4473	0.4831	0.5433
	Sech	0.2148	0.2259	0.2564
	Constructed	0.1436	0.1433	0.1533

5.3 *Results of the Bandgap PCFs with Hollow Core*

To further clarify for which fiber structures the constructed function is suitable, two examples featuring the hollow core band gap photonic crystal fiber are simulated. The first example is a hollow core fiber with a matrix index of 1.45 and three layers of holes in a hexagonal pattern. The lattice spacing is $\Lambda = 5\ \mu$m, and the diameter of the holes divided by the lattice spacing is 0.4. The central hole radius is 5.55 μm. In the second example, the diameter of the holes divided by the lattice spacing is 0.8, the other structure parameters are the same as those in the first example.

The fundamental mode fields of the two examples for different wavelengths are shown in Fig. 9. Figure 9(a) through 9(c) shows the fields of the first example. Figure 9(d) through 9(f) are the fields of the second example. For the first example, it is observed that the field in Fig. 9(a) at $\lambda = 3.1\ \mu$m is better confined in the core, and that Fig. 9(b) and 9(c) shows low confinement, which leads to leakage of the mode. In the second example, Fig. 9(e) at $\lambda = 2.9\ \mu$m shows relative high confinement, while Fig. 9(d) and 9(f) has lower confinement. In addition, the hollow core fiber in the first example has lower confinement than that in the second example. Hence, Fig. 9(a) through 9(c) has more leakage of the mode than Fig. 9(d) through 9(f).

Each field in Fig. 9 is approximated by Gauss, Sech, and the constructed function, respectively. The errors of the first example are tabulated in Table 6. The second example's errors are tabulated in Table 7. Both tables demonstrate that the constructed function can approximate the field of the hollow core fiber better than the Gauss and Sech function. However, because there is more leakage of the mode in the first example, the errors in Table 6 are larger than those in Table 7. Consequently, we don't suggest replacing the actual fundamental mode field with these three functions when large leakage of the mode occurs in the hollow core fiber. But if the replacement is inevitable, our constructed function is recommended. For the hollow core fiber with high field confinement in the core, from Table 7, the constructed function still has better performance than the Gauss and Sech function.

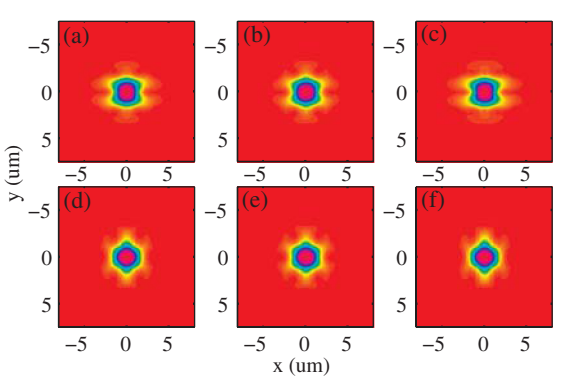

Fig. 8 Fundamental mode fields of PCFs with different elliptical air holes when $r = 0.69\ \mu$m. The orientation of (a)–(c) is 0 deg. The orientation of (d)–(f) is 90 deg. (a) and (d): $r_{maj} = 0.9523\ \mu$m, $r_{min} = 0.5\ \mu$m, (b) and (e): $r_{maj} = 0.794\ \mu$m, $r_{min} = 0.6\ \mu$m, (c) and (f): $r_{maj} = 1.0458\ \mu$m, $r_{min} = 0.45\ \mu$m.

6 Analytic Expression of the Approximated Far Field

In the polar coordinates, the constructed function has the form of

$$f(\rho) = \left(\frac{1}{1+\xi\rho^2}\right)^M, \tag{15}$$

where $x = \rho\cos\theta$ and $y = \rho\sin\theta$. Equation (15) has circular symmetry[30] and its Fourier transform can be represented by

$$F(r) = 2\pi\int_0^\infty \rho(1+\xi\rho^2)^{-M}J_0(2\pi r\rho)\mathrm{d}\rho. \tag{16}$$

If $r = 0$, Eq. (16) becomes

$$F(0) = 2\pi\int_0^\infty \rho(1+\xi\rho^2)^{-M}\mathrm{d}\rho = \frac{\pi}{\xi(M-1)}. \tag{17}$$

If $r > 0$, Eq. (16) becomes

$$F(r) = \frac{2\pi}{\xi^M}\int_0^\infty \frac{J_0(2\pi r\rho)\cdot\rho}{[\rho^2+(\sqrt{1/\xi})^2]^M}\mathrm{d}\rho. \tag{18}$$

Recalling the integral formula[31]

Table 5 Approximation errors for various configurations and orientations when $r = 0.69\ \mu$m.

Orientation	Function	Configuration I $r_{maj} = 0.794\ \mu$m, $r_{min} = 0.6\ \mu$m	Configuration II $r_{maj} = 0.9523\ \mu$m, $r_{min} = 0.5\ \mu$m	Configuration III $r_{maj} = 1.0458\ \mu$m, $r_{min} = 0.45\ \mu$m
0 deg	Gauss	0.0614	0.0779	0.0965
	Sech	0.1359	0.1537	0.1682
	Constructed	0.0628	0.0787	0.0968
90 deg	Gauss	0.0496	0.0489	0.0495
	Sech	0.1159	0.1045	0.0975
	Constructed	0.0514	0.0506	0.0511

$$\int_0^{\infty} \frac{J_\nu(bx)\cdot x^{\nu+1}}{(x^2+a^2)^{\mu+1}}\mathrm{d}x = \frac{a^{\nu-\mu}\cdot b^{\mu}}{2^{\mu}\cdot\Gamma(\mu+1)}\cdot K_{\nu-\mu}(ab) \quad [-1 < \mathrm{Re}\nu < \mathrm{Re}(2\mu+3/2), a>0, b>0], \tag{19}$$

where $K_{\nu-\mu}(\cdot)$ is the second kind modified Bessel function, $\Gamma(\cdot)$ is Gamma function, then, Eq. (18) changes to

$$F(r) = \frac{2\pi^M r^{M-1}}{(\sqrt{\xi})^{M+1}\Gamma(M)} K_{-(M-1)}\left(2\pi r\sqrt{\frac{1}{\xi}}\right). \tag{20}$$

The far field of the fundamental mode field is determined by Fraunhofer diffraction, and the Fraunhofer diffraction equation[30] is

$$U(x_2,y_2) = \frac{\exp(ik\Delta z)\exp[ik(x_2^2+y_2^2)/(2\Delta z)]}{i\lambda\Delta z} F\{U(x_1,y_1)\}, \tag{21}$$

where $F\{\bullet\}$ denotes Fourier transform. Substituting Eq. (17) and (20) into Eq. (21), the analytic expression of the approximated far field in the polar coordinates can be obtained.

$$U(r) = \begin{cases} \dfrac{\exp(ik\Delta z)\exp[ikr^2/(2\Delta z)]}{i\lambda\Delta z}\cdot\dfrac{\pi}{\xi(M-1)}, r=0 \\ \dfrac{\exp(ik\Delta z)\exp[ikr^2/(2\Delta z)]}{i\lambda\Delta z}\cdot\dfrac{2\pi^M r^{M-1}}{(\sqrt{\xi})^{M+1}\Gamma(M)} K_{-(M-1)}\left(2\pi r\sqrt{\dfrac{1}{\xi}}\right), r>0 \end{cases}. \tag{22}$$

7 Numerical Results of the Analytic Expression

For the actual mode fields of PCFs with different d/Λ values and the corresponding approximated fields by the constructed function, we have computed the far fields of these two kinds of fields propagating 1550 μm in free space. The far fields of the approximated fields are computed by Eq. (22). The far field patterns of $d/\Lambda = 0.2$ and $d/\Lambda = 0.6$ are shown in Fig. 10. We can see that the far field patterns of the approximated fields do not have side-lobes. The far field patterns of the actual mode fields have side-lobes with little energy around the center-lobe. However, the energy of side-lobes is so small that the least square errors between the far fields of the approximated field and the far fields of the actual mode fields are very small. The curve of least square errors between these two kinds of far fields is

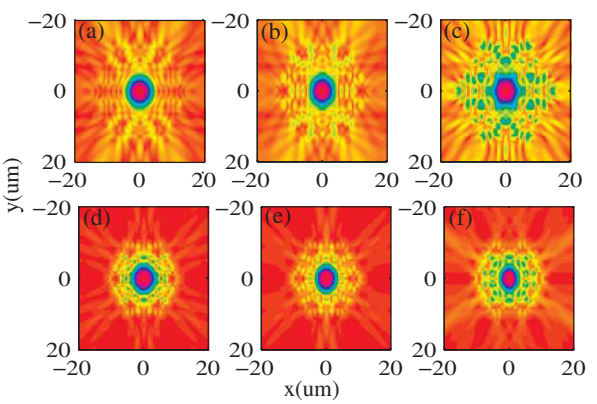

Fig. 9 Fundamental mode fields of the two examples. (a) $\lambda = 3.1\ \mu$m, (b) $\lambda = 3.3\ \mu$m, (c) $\lambda = 3.4\ \mu$m, (d) $\lambda = 2.8\ \mu$m, (e) $\lambda = 2.9\ \mu$m, (f) $\lambda = 3.0\ \mu$m. The first example: (a)–(c); the second example: (d)–(f).

Table 6 Approximation errors of different functions at different wavelengths for the first example.

λ(um)	Gauss	Sech	Constructed function	(ξ, M)
3.1	10.4503	8.98210	4.7848	(0.0890,1.0)
3.3	16.5091	14.0693	6.9937	(0.0772,1.0)
3.4	35.3264	25.5393	12.9633	(0.0370,1.0)

Table 7 Approximation errors of different functions at different wavelengths for the second example.

λ(um)	Gauss	Sech	Constructed function	(ξ, M)
2.8	3.5723	2.3897	1.7214	(0.0625,1.4)
2.9	3.1304	2.1810	1.3755	(0.0865,1.3)
3.0	7.8107	5.5788	2.6472	(0.1111,1.0)

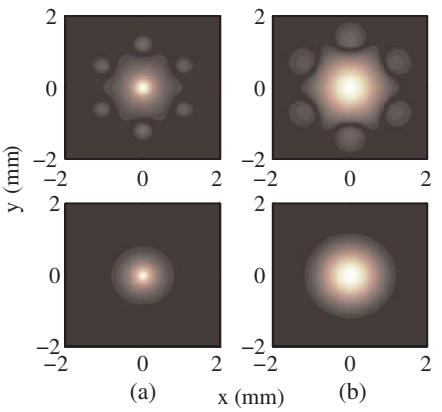

Fig. 10 Far fields of the actual PCFs' fields (above) and far fields of approximated fields by constructed function (below). (a) $d/\Lambda = 0.2$ (b) $d/\Lambda = 0.6$. ($\lambda = 1.55$ μm).

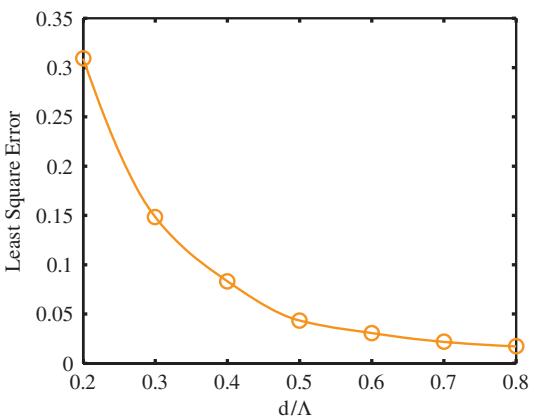

Fig. 11 Least square errors between far fields of the actual PCFs' fields and far fields of approximated fields by constructed function.

plotted in Fig. 11. From Fig. 11, we can see that the errors are small and analogy with that in Fig. 2.

8 Conclusion

In this paper, we constructed a function to approximate the fundamental mode fields of PCFs with different d/Λ values. For PCFs with small d/Λ values, the constructed function approximates the fundamental mode fields in the core precisely, and approximates the fields distributing around the air holes with relative small errors. As a result, the approximation errors brought by the constructed function are smaller than those brought by the Gaussian and Sech function. For PCFs with large d/Λ values, the constructed function approximates the fundamental mode fields with high accuracy, and the approximation errors brought by the constructed function are very close to those brought by the Gaussian function. The constructed function is suitable for PCFs with different structures, which has been proved by the examples of elliptical air holes PCFs and hollow core bandgap PCFs used in the paper. Based on the constructed function, an analytic expression for the far field of the approximated fundamental field is derived. The least square error between the analytic expression and the actual far field is very small. Hence, the analytic expression can represent the actual far field accurately.

Acknowledgments

The authors are grateful for support from the Innovation Project of Chinese Academy of Sciences. And the authors acknowledge Min Zhu for check support and helpful discussion.

Appendix A: Explanations for the Selection of the Intervals of the Optimum Solution of Eq. (9)

In the intervals of $\xi \in (0, +\infty)$, $M \in (0, +\infty)$, according to the fist-order Kuhn-Tucker necessary condition,[24] there are

$$\frac{\partial L}{\partial \xi} = \left.\frac{\partial I(\xi, M)}{\partial \xi}\right|_{(\xi_{\text{opt}}, M_{\text{opt}})} - \mu_1^* = 0, \tag{23}$$

$$\frac{\partial L}{\partial M} = \left.\frac{\partial I(\xi, M)}{\partial M}\right|_{(\xi_{\text{opt}}, M_{\text{opt}})} - \mu_2^* = 0. \tag{24}$$

In the Cartesian coordinates, Eq. (23) is

$$\begin{aligned}\frac{\partial L}{\partial \xi} = {} & 2M_{\text{opt}} \int_{-\infty}^{+\infty}\int_{-\infty}^{+\infty} \phi(x,y)[1+\xi_{\text{opt}}(x^2+y^2)]^{-M_{\text{opt}}-1} \\ & \times (x^2+y^2)\mathrm{d}x\mathrm{d}y - 2M_{\text{opt}} \int_{-\infty}^{+\infty}\int_{-\infty}^{+\infty} \\ & \times [1+\xi_{\text{opt}}(x^2+y^2)]^{-2M_{\text{opt}}-1} \\ & \times (x^2+y^2)\mathrm{d}x\mathrm{d}y - \mu_1^* = 0.\end{aligned} \tag{25}$$

For the second integral in Eq. (25), we replace x, y with $\rho \cos\theta$ and $\rho \sin\theta$, then

$$\begin{aligned}&\int_{-\infty}^{+\infty}\int_{-\infty}^{+\infty} [1+\xi_{\text{opt}}(x^2+y^2)]^{-2M_{\text{opt}}-1}(x^2+y^2)\mathrm{d}x\mathrm{d}y \\ &= \pi \int_0^{+\infty} (1+\xi_{\text{opt}}\rho^2)^{-2M_{\text{opt}}-1}\rho^2 \mathrm{d}\rho^2.\end{aligned} \tag{26}$$

Substituting ρ^2 with t, Eq. (26) changes to $\pi\int_0^{+\infty}(1+\xi_{\text{opt}}t)^{-2M_{\text{opt}}-1}t\mathrm{d}t$, then integrating this term yields

$$\pi\int_0^{+\infty}(1+\xi_{\mathrm{opt}}t)^{-2M_{\mathrm{opt}}-1}t\mathrm{d}t = -\frac{\pi}{2\xi_{\mathrm{opt}}M_{\mathrm{opt}}}\left\{\lim_{t\to+\infty}t(1+\xi_{\mathrm{opt}}t)^{-2M_{\mathrm{opt}}} + \frac{1}{\xi_{\mathrm{opt}}(2M_{\mathrm{opt}}-1)}\left[\lim_{t\to+\infty}(1+\xi_{\mathrm{opt}}t)^{-2M_{\mathrm{opt}}+1}-1\right]\right\}. \tag{27}$$

For Eq. (27), only if $M_{\mathrm{opt}} \geq 1/2$, the limits exist, thus, Eq. (23) makes sense.

In the Cartesian coordinates, Eq. (24) is

$$\frac{\partial L}{\partial M} = 2\int_{-\infty}^{+\infty}\int_{-\infty}^{+\infty}\phi(x,y)[1+\xi_{\mathrm{opt}}(x^2+y^2)]^{-M_{\mathrm{opt}}} \times \ln[1+\xi_{\mathrm{opt}}(x^2+y^2)]\mathrm{d}x\mathrm{d}y - 2\int_{-\infty}^{+\infty}\int_{-\infty}^{+\infty}[1+\xi_{\mathrm{opt}}(x^2+y^2)]^{-2M_{\mathrm{opt}}} \times \ln[1+\xi_{\mathrm{opt}}(x^2+y^2)]\mathrm{d}x\mathrm{d}y - \mu_2^* = 0. \tag{28}$$

For the second integral in Eq. (28), we replace x, y with $\rho\cos\theta$ and $\rho\sin\theta$, then

$$\int_{-\infty}^{+\infty}\int_{-\infty}^{+\infty}[1+\xi_{\mathrm{opt}}(x^2+y^2)]^{-2M_{\mathrm{opt}}}\ln[1+\xi_{\mathrm{opt}}(x^2+y^2)]\mathrm{d}x\mathrm{d}y = \pi\int_0^{+\infty}(1+\xi_{\mathrm{opt}}\rho^2)^{-2M_{\mathrm{opt}}}\ln(1+\xi_{\mathrm{opt}}\rho^2)\mathrm{d}\rho^2. \tag{29}$$

If $\xi_{\mathrm{opt}} > 0$, Eq. (29) becomes

$$\pi\int_0^{+\infty}(1+\xi_{\mathrm{opt}}\rho^2)^{-2M_{\mathrm{opt}}}\ln(1+\xi_{\mathrm{opt}}\rho^2)\mathrm{d}\rho^2 = \frac{\pi}{\xi_{\mathrm{opt}}}\int_1^{+\infty}(1+\xi_{\mathrm{opt}}\rho^2)^{-2M_{\mathrm{opt}}}\ln(1+\xi_{\mathrm{opt}}\rho^2)\mathrm{d}(1+\xi_{\mathrm{opt}}\rho^2). \tag{30}$$

Let $t = 1+\xi_{\mathrm{opt}}\rho^2$, Eq. (30) changes to

$$\frac{\pi}{\xi_{\mathrm{opt}}}\int_1^{+\infty}(1+\xi_{\mathrm{opt}}\rho^2)^{-2M_{\mathrm{opt}}}\ln(1+\xi_{\mathrm{opt}}\rho^2)\mathrm{d}(1+\xi_{\mathrm{opt}}\rho^2) = \frac{\pi}{\xi_{\mathrm{opt}}}\int_1^{+\infty}t^{-2M_{\mathrm{opt}}}\ln(t)\mathrm{d}t. \tag{31}$$

Integrating Eq. (31) yields

$$\frac{\pi}{\xi_{\mathrm{opt}}}\int_1^{+\infty}t^{-2M_{\mathrm{opt}}}\ln(t)\mathrm{d}t = \frac{\pi}{\xi_{\mathrm{opt}}(-2M_{\mathrm{opt}}+1)}\left\{\lim_{t\to+\infty}[t^{-2M_{\mathrm{opt}}+1}\ln(t)] + \frac{1}{2M_{\mathrm{opt}}-1}\left[\lim_{t\to+\infty}(t^{-2M_{\mathrm{opt}}+1})-1\right]\right\}. \tag{32}$$

For Eq. (32), only if $M_{\mathrm{opt}} > 1/2$, the limits exist, therefore, Eq. (24) makes sense.

From the above discussion, only if $\xi_{\mathrm{opt}} > 0$ and $M_{\mathrm{opt}} > 1/2$, Eqs. (23) and (24) just make sense at the same time. So the intervals are $\xi_{\mathrm{opt}} > 0$ and $M_{\mathrm{opt}} > 1/2$.

Appendix B: Explanations for the Selection of the Intervals of the Optimum Solution of Eq. (12)

For $\xi, M \in \mathbb{R}^n$, based on the assumption that $I(\xi, M)$ possesses continuous first and second partial derivatives with respect to ξ_{opt} and M_{opt}, according to the first-order necessary condition of unconstrained nonlinear programming,[24] there are

$$\left.\frac{\partial I(\xi,M)}{\partial\xi}\right|_{(\xi_{\mathrm{opt}},M_{\mathrm{opt}})} = 0, \tag{33}$$

$$\left.\frac{\partial I(\xi,M)}{\partial M}\right|_{(\xi_{\mathrm{opt}},M_{\mathrm{opt}})} = 0. \tag{34}$$

In the Cartesian coordinates, Eq. (33) is

$$\left.\frac{\partial I(\xi,M)}{\partial\xi}\right|_{(\xi_{\mathrm{opt}},M_{\mathrm{opt}})} = 2M_{\mathrm{opt}}\int_{-\infty}^{+\infty}\int_{-\infty}^{+\infty}\phi(x,y) \times [1+\xi_{\mathrm{opt}}(x^2+y^2)]^{-M_{\mathrm{opt}}-1}(x^2+y^2)\mathrm{d}x\mathrm{d}y - 2M_{\mathrm{opt}}\int_{-\infty}^{+\infty}\int_{-\infty}^{+\infty}[1+\xi_{\mathrm{opt}}(x^2+y^2)]^{-2M_{\mathrm{opt}}-1} \times (x^2+y^2)\mathrm{d}x\mathrm{d}y = 0. \tag{35}$$

If $\xi_{\mathrm{opt}} = 0$, the second integral in Eq. (35) changes to $\int_{-\infty}^{+\infty}\int_{-\infty}^{+\infty}(x^2+y^2)\mathrm{d}x\mathrm{d}y$. This term is infinite, thus Eq. (35) makes no sense, so $\xi_{\mathrm{opt}} \neq 0$. For $\xi_{\mathrm{opt}} \neq 0$, after integrating the second integral in Eq. (35), the result is the same as Eq. (27). So only if $M_{\mathrm{opt}} \geq 1/2$, Eq. (35) makes sense and Eq. (33) can just be satisfied.

In the Cartesian coordinates, Eq. (34) is

$$\left.\frac{\partial I(\xi,M)}{\partial M}\right|_{(\xi_{\mathrm{opt}},M_{\mathrm{opt}})} = 2\int_{-\infty}^{+\infty}\int_{-\infty}^{+\infty}\phi(x,y) \times [1+\xi_{\mathrm{opt}}(x^2+y^2)]^{-M_{\mathrm{opt}}}\ln[1+\xi_{\mathrm{opt}}(x^2+y^2)]\mathrm{d}x\mathrm{d}y - 2\int_{-\infty}^{+\infty}\int_{-\infty}^{+\infty}[1+\xi_{\mathrm{opt}}(x^2+y^2)]^{-2M_{\mathrm{opt}}} \times \ln[1+\xi_{\mathrm{opt}}(x^2+y^2)]\mathrm{d}x\mathrm{d}y = 0. \tag{36}$$

According to the above discussion, $\xi_{\mathrm{opt}} \neq 0$. If $\xi_{\mathrm{opt}} < 0$, for the second integral in Eq. (36), we replace x, y with $\rho\cos\theta$ and $\rho\sin\theta$, then

$$\int_{-\infty}^{+\infty}\int_{-\infty}^{+\infty}[1+\xi_{\mathrm{opt}}(x^2+y^2)]^{-2M_{\mathrm{opt}}} \times \ln[1+\xi_{\mathrm{opt}}(x^2+y^2)]\mathrm{d}x\mathrm{d}y = \pi\int_0^{+\infty} \times (1+\xi_{\mathrm{opt}}\rho^2)^{-2M_{\mathrm{opt}}}\ln(1+\xi_{\mathrm{opt}}\rho^2)\mathrm{d}\rho^2. \tag{37}$$

Let $t = 1+\xi_{\mathrm{opt}}\rho^2$, Eq. (37) becomes

$$\pi \int_0^{+\infty} (1+\xi_{\text{opt}}\rho^2)^{-2M_{\text{opt}}} \ln(1+\xi_{\text{opt}}\rho^2)\mathrm{d}\rho^2 = \frac{\pi}{\xi_{\text{opt}}} \int_0^1 t^{-2M_{\text{opt}}} \ln(t)\mathrm{d}t. \quad (38)$$

Integrating Eq. (38) yields

$$\frac{\pi}{\xi_{\text{opt}}} \int_0^1 t^{-2M_{\text{opt}}} \ln(t)\mathrm{d}t = \frac{\pi}{\xi_{\text{opt}}(-2M_{\text{opt}}+1)} \times \left\{ -\lim_{t\to 0}[t^{-2M_{\text{opt}}+1}\ln(t)] - \frac{1}{2M_{\text{opt}}-1}[\lim_{t\to 0}(t^{-2M_{\text{opt}}+1})-1] \right\}. \quad (39)$$

For Eq. (39), only if $M_{\text{opt}} < 1/2$, the limits exist, therefore, Eq. (34) makes sense. If $\xi_{\text{opt}} > 0$, after integrating the second integral in Eq. (14), the result is the same as Eq. (32), so only if $M_{\text{opt}} > 1/2$, Eq. (36) makes sense and Eq. (34) can just be satisfied.

According to the above discussion, only if $\xi_{\text{opt}} > 0$ and $M_{\text{opt}} > 1/2$, Eqs. (33) and (34) just make sense at the same time. So the intervals becomes $\xi_{\text{opt}} > 0$, $M_{\text{opt}} > 1/2$.

References

1. J. C. Knight et al., "All-silica single-mode optical fiber with photonic crystal cladding," *Opt. Lett.* **21**(19), 1547–1549 (1996).
2. S. Lu et al., "Analysis of birefringent and dispersive properties of photonic crystal fibers," *Appl. Opt.* **50**(30), 5798–5802 (2011).
3. X. M. Xi et al., "Mode-field expansion in photonic crystal fibers," *Appl. Opt.* **50**(25), E50–E54 (2011).
4. T. Hirooka, Y. Hori, and M. Nakazawa, "Gaussian and Sech approximations of mode field profiles in photonic crystal fibers," *IEEE Photonics Techonol. Lett.* **16**(4), 1071–1073 (2004).
5. R. E. Wagner and W. J. Tomlinson, "Coupling efficiency of optics in single-mode fiber components," *Appl. Opt.* **21**(15), 2671–2687 (1982).
6. C. Ruilier and F. Cassaing, "Coupling of large telescope and single-mode waveguides: application to stellar interferometry," *J. Opt. Soc. Am. A* **18**(1), 143–149 (2001).
7. O. Wallner, P. J. Winzer, and W. R. Leeb, "Alignment tolerances for plane-wave to single-mode fiber coupling and their mitigation by use of pigtailed collimators," *Appl. Opt.* **41**(4), 637–643 (2002).
8. Y. Dikmelik and F. M. Davidson, "Fiber-coupling efficiency for free-space optical communication through atmospheric turbulence," *Appl. Opt.* **44**(23), 4946–4952 (2005).
9. M. Toyoshima, "Maximum fiber coupling efficiency and optimum beam size in the presence of random angular jitter for free-space laser systems and their applications," *J. Opt. Soc. Am. A* **23**(9), 2246–2250 (2006).
10. J. Ma et al., "Plane wave coupling into single-mode fiber in the presence of random angular jitter," *Appl. Opt.* **48**(27), 5184–5189 (2009).
11. Ch. Y. Chen et al., "Coupling plane wave received by an annular aperture into a single-mode fiber in the presence of atmospheric turbulence," *Appl. Opt.* **50**(3), 307–312 (2011).
12. J. C. W. Corbett and J. R. Allington-Smith, "Coupling starlight into single-mode photonic crystal fiber using a field lens," *Opt. Express* **13**(17), 6527–6540 (2005).
13. J. C. W. Corbett et al., "The coupling performance of photonic crystal fibers in fibre stellar interferometry," *Mon. Not. R. Astron. Soc.* **368**(1), 203–210 (2006).
14. J. C. W. Corbett, T. J. Morris, and J. R. Allington-Smith, "Tip-tilt requirements for coupling starlight into single-mode photonic crystal fibres using a lenslet: a first analysis," *New Astron. Rev.* **49**(12), 675–680 (2006).
15. C. Poppett and J. Allington-Smith, "Coupling efficiency and termination of photonic crystal fibres for astronomy," *Proc. SPIE* **7018**, 1–10 (2008).
16. M. Koshiba and K. Saitoh, "Structural dependence of effective area and mode field diameter for holey fibers," *Opt. Express* **11**(15), 1746–1756 (2003).
17. N. A. Mortensen et al., "Modal cutoff and the V parameter in photonic crystal fibers," *Opt. Lett.* **28**(20), 1879–1881 (2003).
18. J. R. Folkenberg et al., "Experimental investigation of cutoff phenomena in nonlinear photonic crystal fibers," *Opt. Lett.* **28**(20), 1882–1884 (2003).
19. A. Sharma and H. Chauhan, "A new analytical model for the field of microstructured optical fibers," *Opt. Quant. Electron.* **41**(4), 235–242 (2009).
20. D. Ghosh, S. Roy, and S. K. Bhadra, "Determination of modal effective indices and dispersion of microstructured fibers with different configurations: a variational approach," *J. Mod. Opt.* **57**(8), 607–620 (2010).
21. A. Bondeson, T. Rylander, and P. Ingelstrom *Compuational Electromagnetics*, Springer Science+Business Media, Inc., New York (2005).
22. L. Zhang et al., "Study of time-domain spreading model of ultrafast Gaussian laser pulses in atmospheric turbulence," *Acta. Opt. Sin.* **32**(4), 1–6 (2012).
23. W. M. Wells, "Efficient synthesis of Gaussian filters by cascaded uniform filters," *IEEE Trans. Pattern Anal. Mach. Intell.* **PAMI-8** (2), 234–239 (1986).
24. U. Diwekar, *Introduction to Applied Optimization*, Springer Science +Business Media, LLC., New York (2008).
25. D. G. Luenberger and Y. Y. Ye, *Linear and Nonlinear Programming*, Third Edition, Springer Science+Business Media, LLC., New York (2008).
26. http://sydney.edu.au/science/physics/cudos/research/mofsoftware.shtml.
27. T. P. White et al., "Multipole method for microstructured optical fibers I. Formulation," *J. Opt. Soc. Am. B* **19**(10), 2322–2330 (2002).
28. B. T. Kuhlmey et al., "Multipole method for microstructured optical fibers. II. Implementation and results," *J. Opt. Soc. Am. B* **19**(10), 2331–2340 (2002).
29. R. Sharma, V. Janyani, and S. K. Bhatnagar, "Improved single mode property in elliptical air hole photonic crystal fiber," *J. Mod. Opt.* **58**(7), 604–610 (2011).
30. J. W. Goodman *Introduction to Fourier Optics*, Second Edition, The McGraw-Hill Companies, Inc., New York (1995).
31. I. S. Gradshteyn and I. M. Ryzhik, *Table of Integrals, Series, and Products* Seventh Edition, Elsevier Academic Press, San Diego (2007).

Lu Zhang received his BS in electrical engineering from Northeast Normal University, Changchun, China, in 2008. He is currently a PhD student in Circuits and Systems at Changchun Institute of Optics, Fine Mechanics and Physics, Chinese Academy of Sciences. His current research interests include fiber optics, free-space optical communications, laser beam propagation in atmospheric turbulence, and optical coherent detection.

Zhiyong Wu received his BS in electronics engineering from Changchun University of Science and Technology, Changchun, China, in 1989. He is currently a professor in Circuits and Systems at Changchun Institute of Optics, Fine Mechanics and Physics, Chinese Academy of Sciences. His current research interests include laser ranging, free-space optical communications, and EO theodolite.

Shijie Gao received his BS in electronics engineering from Harbin University of Science and Technology, Harbin, China. He received his MS at Changchun Institute of Optics, Fine Mechanics and Physics, Chinese Academy of Sciences. He is currently an assistant researcher. His current research interests are free-space optical communications and optical coherent detection.

Ming Cui received his BS in communication engineering from Jilin University, Changchun, China and received his MS at Changchun Institute of Optics, Fine Mechanics and Physics, Chinese Academy of Sciences. He is currently a PhD student at Changchun Institute of Optics, Fine Mechanics and Physics, Chinese Academy of Sciences. His current research interests are free-space optical communications and optical coherent detection.